Reversal of the transverse force on a spherical bubble rising close to a vertical wall at moderate-to-high Reynolds numbers

Pengyu Shi

Reversal of the transverse force on a spherical bubble rising close to a vertical wall at moderate-to-high Reynolds numbers

Pengyu Shi *

Helmholtz-Zentrum Dresden–Rossendorf, Institute of Fluid Dynamics, Bautzner Landstrasse 400, D-01328 Dresden, Germany and Institut de Mécanique des Fluides de Toulouse (IMFT), Université de Toulouse, CNRS, 31400 Toulouse, France

(Received 14 October 2023; accepted 8 January 2024; published 6 February 2024)

The flow past a clean spherical bubble translating steadily parallel to a no-slip wall in a stagnant fluid is studied numerically over a wide range of moderate-to-high Reynolds numbers. We focus on situations where the distance separating the bubble from the wall is smaller than the size of the bubble to explore the competition between viscous and inertial effects in the gap. More precisely, the range of the wall distance considered is $1.1 \leqslant L_{\mathrm{R}} \leqslant 2$ (L_{R} being the distance from the bubble center to the wall normalized by the bubble radius), and that of the Reynolds number is $50 \leqslant \mathrm{Re} \leqslant 1000$ (Re being based on the bubble diameter and the slip velocity). In contrast to predictions based on potential flow theory, the numerical results reveal that, when the gap is smaller than a critical value that depends on the Reynolds number, the transverse force starts to decrease with decreasing separation and may finally reverse, changing from attractive to repulsive. This effect is found to be due to the strong shear generated in the gap, which, combined with the local transverse gradient of the streamwise velocity, results in a system of two counterrotating streamwise vortices and, consequently, a shear-induced lift pointing away from the wall. Computational results together with available high-Reynolds-number theory provide empirical expressions for the drag and transverse forces in the steady-state limit. Then the competition between the various transverse forces on a bubble bouncing close to the wall is examined, based on previously measured data for bubble trajectory. The central role of the history effects due to the misalignment between the wake and the instantaneous angle of the bubble path is confirmed. Computational results also reveal that, depending on the initial separation, a freely moving bubble may either reach a stable equilibrium position close to the wall or depart from the wall up to infinity.

DOI: 10.1103/PhysRevFluids.9.023601

I. INTRODUCTION

At moderate-to-high Reynolds numbers, a clean (i.e., surfactant-free) spherical bubble rising in a stagnant fluid bounded by a vertical wall is known to migrate towards the wall, provided that the initial separation is not too large. However, when the separation distance is small enough, the bubble is observed to bounce very close to the wall [1–3]. The migration toward the wall is well predicted by potential flow theory: the relative fluid velocity reaches a maximum in the gap, thus inducing an attractive transverse force, owing to the irrotational mechanism [4–6]. The bouncing motion can be purely hydrodynamical, as the transverse force reverses when the bubble stands very close to

* p.shi@hzdr.de

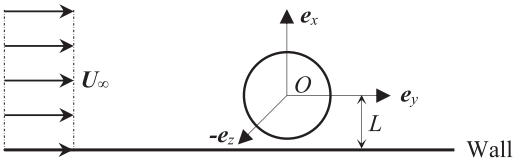

FIG. 1. Schematic of a bubble moving parallel to a wall in a stagnant fluid.

the wall without touching it [3,7]. Therefore, it is expected that the flow in the gap, which becomes dominated by viscous effects when the separation is small enough, is responsible for this reversal.

A detailed understanding of the various mechanisms at play is difficult, since the lateral force balance on a bouncing bubble also involves time-dependent contributions resulting from the time variations of the flow disturbance [3,8]. As a first step towards a complete description of the phenomenon, we consider the flow past a spherical bubble moving steadily parallel to a wall in a stagnant fluid. By considering separation distances much smaller than the bubble radius, we expect to cover the transition from the attractive behavior to the near-wall repulsive behavior. The computational results for the drag and lift forces obtained in the steady-flow limit, together with the measured trajectory of a bouncing bubble from Ref. [3], are then used to evaluate the time-dependent contributions, in particular the history effects, to the lateral force balance. The results provided in this paper also provide a good starting point for the investigation of more complex near-wall bouncing motions, including, e.g., bubble-wall collision [9], bubble deformation [10], and bubble clustering [11].

The paper is organized as follows. In Sec. II we formulate the problem, specify the considered range of parameters, and outline the numerical approach, which is essentially similar to that employed in Refs. [12,13]. Section III discusses the evolution of the velocity and vorticity fields with the wall distance and Reynolds number. Section IV is devoted to an extensive analysis of the numerical results obtained for the hydrodynamic forces acting on the bubble. Concluding remarks are given in Sec. V.

II. STATEMENT OF THE PROBLEM AND OUTLINE OF THE NUMERICAL APPROACH

In this study, we examine the steady-state hydrodynamic force acting on a clean spherical bubble rising parallel to a wall in a stationary liquid. The problem is analyzed in a reference frame moving with the bubble, rendering the bubble stationary while the surrounding fluid and the no-slip wall move at a constant velocity. We define a Cartesian coordinate system $(Oxyz)$ with the origin located at the center of the bubble, as illustrated in Fig. 1. In this coordinate system, the bubble is stationary, and the ambient flow is $\boldsymbol{U}_\infty = U_\infty \boldsymbol{e}_y$. The wall is located at $x = -L$, and $\boldsymbol{e}_x$ denotes the wall-normal unit vector pointing into the fluid. The fluid velocity and pressure fields in the presence of the bubble are denoted by $\boldsymbol{u}$ and p, respectively, and $\boldsymbol{\omega} = \boldsymbol{\nabla} \times \boldsymbol{u}$ denotes the vorticity.

The flow past the bubble is assumed to be governed by the incompressible Navier-Stokes equations:

$$\boldsymbol{\nabla} \cdot \boldsymbol{u} = 0, \quad \frac{\partial \boldsymbol{u}}{\partial t} + \boldsymbol{u} \cdot \boldsymbol{\nabla} \boldsymbol{u} = -\frac{1}{\rho} \boldsymbol{\nabla} p + \boldsymbol{\nabla} \cdot \boldsymbol{\tau}, \tag{1a,b}$$

where $\boldsymbol{\tau} = \nu[\boldsymbol{\nabla} \boldsymbol{u} + {}^T \boldsymbol{\nabla} \boldsymbol{u}]$ is the viscous part of the stress tensor $\boldsymbol{\Sigma} = -p\boldsymbol{I} + \rho\boldsymbol{\tau}$, and ρ is the fluid density, with $\boldsymbol{I}$ denoting the Kronecker tensor. In the reference frame attached to the center of the bubble, the disturbance vanishes both at the wall and in the region far away from the bubble, namely,

$$\boldsymbol{u} = U_\infty \boldsymbol{e}_y \quad \text{for} \quad x = -L \cup r \to \infty, \tag{2}$$

where $r = (x^2 + y^2 + z^2)^{1/2}$ denotes the distance to the bubble center. On the bubble surface, the normal velocity must vanish, owing to the nonpenetration condition. Moreover, the dynamic

viscosity of the gas within the bubble is assumed to be much smaller than that of the ambient liquid, and the bubble surface is considered to be free of any surfactant, so that the outer fluid adheres to a shear-free condition at the interface. Last, we assume the surface tension is strong enough for the capillary force to maintain the bubble's sphericity, regardless of the local strength of the hydrodynamic stresses. Under such conditions, the boundary conditions at the bubble surface are

$$\left.\begin{array}{l} \boldsymbol{u}\cdot\boldsymbol{n}=0 \\ \boldsymbol{n}\times(\boldsymbol{\tau}\cdot\boldsymbol{n})=0 \end{array}\right\} \quad \text{for} \quad r=R, \tag{3}$$

where $\boldsymbol{n}$ denotes the outward unit normal to the bubble surface and R is the bubble radius. Under the above boundary conditions, the steady solution of the problem depends on two characteristic parameters: namely, the Reynolds number Re and the wall distance L_{R}. They are defined as

$$\mathrm{Re}=\frac{U_\infty(2R)}{\nu}, \quad L_{\mathrm{R}}=\frac{L}{R}. \tag{4}$$

To achieve a systematic investigation, we have considered $10 \leqslant \mathrm{Re} \leqslant 1000$ and $1.1 \leqslant L_{\mathrm{R}} \leqslant 10$. Nevertheless, a majority of the results presented herein focus on $50 \leqslant \mathrm{Re} \leqslant 1000$ and $1.1 \leqslant L_{\mathrm{R}} \leqslant 2$ since our aim is to elaborate on the hydrodynamic interaction between the bubble and the wall in the moderate-to-high Re regime.

We are particularly interested in obtaining the hydrodynamic force acting on the bubble. This force may be split into its drag component F_{D}, parallel to $\boldsymbol{e}_y$, and its lift or transverse component F_{L}, parallel to $\boldsymbol{e}_x$. We thus define

$$F_{\mathrm{D}}=\boldsymbol{e}_y\cdot\int_\Gamma \boldsymbol{\Sigma}\cdot\boldsymbol{n}\,d\Gamma, \quad F_{\mathrm{L}}=\boldsymbol{e}_x\cdot\int_\Gamma \boldsymbol{\Sigma}\cdot\boldsymbol{n}\,d\Gamma, \tag{5}$$

where Γ is the bubble surface. Results concerning these forces will be expressed in terms of the dimensionless lift and drag coefficients, C_{L} and C_{D}, obtained by dividing the corresponding component of the force by $\pi R^2\rho U_\infty^2/2$. Note that a negative (respectively, positive) value of the lift coefficient corresponds to an attractive (respectively, repulsive) force with respect to the wall.

The numerical simulations are carried out with the JADIM code developed at IMFT [14–16]. The computational domain is cylindrical, and the bubble center stands on the axis of the cylinder. The no-slip wall coincides with one base of the cylinder, while the unperturbed far field is approached at the other base and at the cylindrical surface. More details about the grid system are given in the Appendix. The reader is referred to Refs. [12,13] for numerical aspects concerning the specificities of the code and the boundary conditions. The major difference in the present problem compared to the previous ones in Refs. [12,13] is that much smaller wall distances have been considered in this work. To properly resolve the boundary layer that develops along the wall, the grid in the gap is highly refined. A systematic grid study was carried out to achieve grid-independent results, as detailed in the Appendix.

III. FLOW AND VORTICITY FIELDS

Figure 2 illustrates the structure of the spanwise vorticity $\omega_z=\boldsymbol{\omega}\cdot\boldsymbol{e}_z$ and the streamline in the symmetry plane $z=0$. Vorticity is generated both at the bubble surface, due to the finite interface curvature, and at the wall, owing to the no-slip condition. In the discussion that follows, the contributions from these two distinct boundaries are designated as surface vorticity and wall vorticity, respectively. The typical structures of these two different vortical contributions can be clearly observed in Fig. 2(c), where the interaction between them is weak, due to the moderate wall distance ($L_{\mathrm{R}}=1.25$) and the high Reynolds number ($\mathrm{Re}=500$) involved. In this case, the surface vorticity exhibits opposite signs depending on x and, for the structure shown in the symmetry plane $z=0$, is nearly symmetric with respect to $x=0$. The wall vorticity features a positive thread (in which $\omega_z>0$) concentrated in the gap and advected away from the wall, and a negative thread that adheres to the wall, spanning a larger distance downstream in the wake. As Re decreases, the

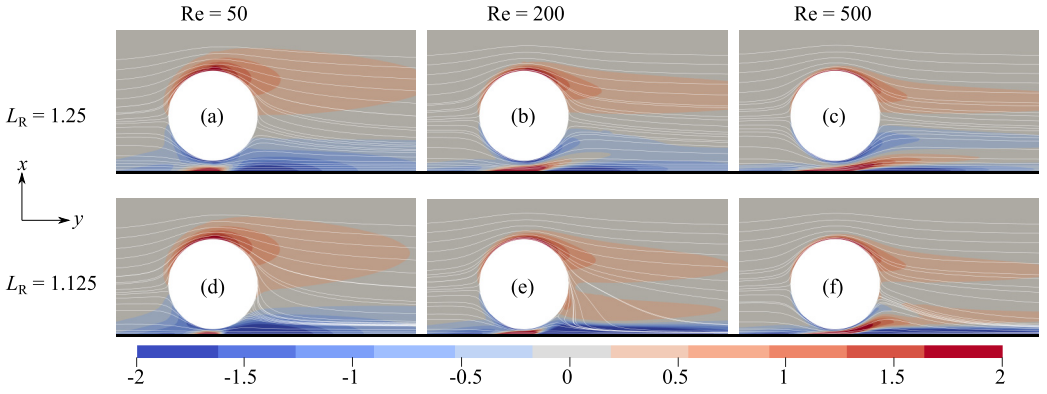

FIG. 2. Isocontours of the normalized spanwise vorticity $(R/U_\infty)\boldsymbol{\omega}\cdot\boldsymbol{e}_z$ as well as the streamlines in the symmetry plane $z = 0$. The wall is situated at the bottom of each panel. The relative flow with respect to the bubble proceeds from left to right.

thicknesses of the boundary layers at the wall and at the bubble surface increase, enhancing the vortical interaction between them. As observed in Figs. 2(a) and 2(b), the two regions containing negative vorticity begin to interpenetrate each other at $\mathrm{Re} = 200$ and become indistinguishable at $\mathrm{Re} = 50$. Furthermore, the presence of the wall attenuates the vorticity generated at the lower half of the bubble, a phenomenon deducible by comparing the two threads of the surface vorticity at $\mathrm{Re} = 200$ [see Fig. 2(b)].

The vortical interaction depicted at $L_\mathrm{R} = 1.125$ differs notably from that at $L_\mathrm{R} = 1.25$. First, it can be observed from the streamlines shown in Figs. 2(d)–2(f) that, downstream in the wake, the fluid elements on the unbounded side are strongly entrained towards negative x, causing the positive surface vorticity to bend towards the wall. Specifically, at $\mathrm{Re} = 200$ and $L_\mathrm{R} = 1.125$ [Fig. 2(e)], this shift is sufficiently pronounced such that the positive surface vorticity reaches the lower half of the bubble and is further advected downwards. Given that the generation of the negative thread of the surface vorticity is substantially suppressed by the wall, the surface vorticity maintains a constant sign in the bubble wake. The shift is not obvious at $\mathrm{Re} = 500$ [Fig. 2(f)], yet the development of the surface vorticity at the lower half of the bubble remains suppressed by the wall. Consequently, the structure of the surface vorticity is strongly asymmetric, which contrasts with the nearly axisymmetric wake structure that persists for $L_\mathrm{R} = 1.25$ [Fig. 2(c)].

Another intriguing perspective of the flow is depicted in Fig. 3, illustrating the distribution of the streamwise relative fluid velocity $u_y = \boldsymbol{u}\cdot\boldsymbol{e}_y$ along the x-axis. According to the potential flow theory, the wall proximity induces an acceleration of the flow in the gap. This is qualitatively validated by the present simulation results at $\mathrm{Re} = 500$, where the maximum velocity exhibits a rapid increase with a decrease in L_R for $L_\mathrm{R} \geqslant 1.15$. Nonetheless, this increment does not persist at smaller separations ($L_\mathrm{R} \leqslant 1.15$), and the maximum velocity even decreases when L_R decreases from 1.125 to 1.1. This contradictory behavior can be attributed to the vortical interaction in the gap [Fig. 2(f)], which attenuates the flow acceleration in the region proximal to the lower half of the bubble. For the same reason, the maximum velocity at a given L_R decreases with decreasing Re. For instance, for $L_\mathrm{R} = 1.125$, this maximum achieves $1.87U_\infty$ at $\mathrm{Re} = 500$, while it is only $1.22U_\infty$ at $\mathrm{Re} = 50$. Additionally, the critical wall distance $L_{\mathrm{R,C1}}(\mathrm{Re})$, below which the maximum velocity start to decrease, increases with a reduction in Re. For instance, we observe that $L_{\mathrm{R,C1}}(200) \approx 1.15$, while $L_{\mathrm{R,C1}}(100) \approx 1.25$. In all scenarios, the velocity on the unbounded side is only marginally influenced by the presence of the wall.

The downward bending (i.e., towards $-x$) of the flow in the wake revealed from Fig. 2 can be better understood by examining the streamwise vorticity, $\omega_y = \boldsymbol{\omega}\cdot\boldsymbol{e}_y$. This is illustrated in Fig. 4,

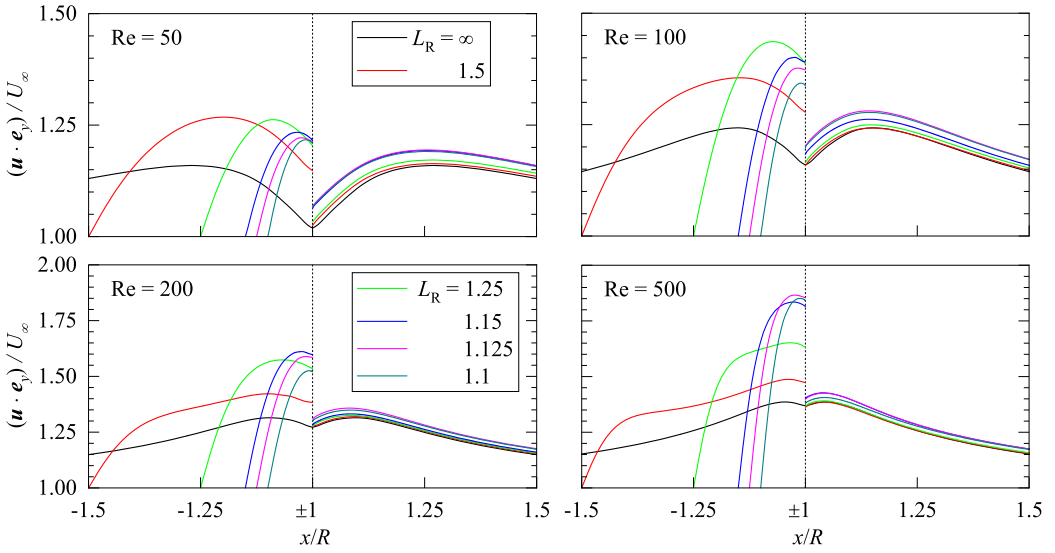

FIG. 3. Distribution of the streamwise relative fluid velocity $\boldsymbol{u} \cdot \boldsymbol{e}_y/U_\infty$ along the x-axis (to enhance the view of the flow in the gap, the $[-1, +1]$ interval of the axis has been omitted, thus shrinking the bubble to a point denoted by $|x/R| = 1$).

which displays the ω_y-distribution in the region excluding the wall boundary layer, i.e., for $x \geqslant -1$. The streamwise vorticity is concentrated within two elongated vortices situated on both sides of the symmetry plane $z = 0$. The fluid located between the two vortex threads is entrained downwards, as revealed from the streamlines shown in Fig. 2. Not shown in Fig. 4 is the ω_y-distribution in the wall boundary layer. As previously discussed in Ref. [12], two counterrotating "pancake" streamwise vortices are present there. The orientation of these two vortices is opposite to their counterparts in the bubble wake. The two pancake vorticities are pronounced in the gap, bending the positive component of the wall vorticity away from the wall, as observed in Fig. 2.

The generation of streamwise vorticity in the wake is closely related to the vortical interaction in the gap, as in the corresponding unbounded case, the flow is axisymmetric irrespective of Re [17]. In the limit $L_R \to 1$, the vortical wall-bubble interaction is pronounced, and the flow in the

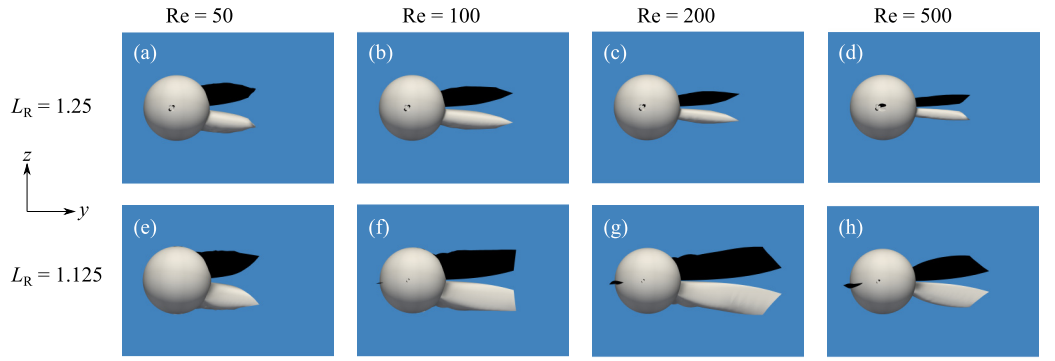

FIG. 4. Isosurfaces $(R/U_\infty)\boldsymbol{\omega} \cdot \boldsymbol{e}_y = \pm 0.15$ of the streamwise vorticity in the bubble wake (the black thread corresponds to positive values). The relative flow is from left to right, while the wall is situated at the back of the bubble.

gap resembles a lubrication flow of Reynolds number

$$\mathrm{Re}_l = \frac{(U_{\max} - U_\infty)(L - R)}{\nu} = \frac{\mathrm{Re}}{2}\left(\frac{U_{\max}}{U_\infty} - 1\right)(L_\mathrm{R} - 1), \tag{6}$$

where $U_{\max}$ is the maximum streamwise relative fluid velocity in the gap. At a given Re, the value of $U_{\max}$ depends only weakly on L_R for $L_\mathrm{R} \leqslant 1.25$ (see Fig. 3). Therefore, the proximity to the wall decreases Re_l, enhancing the vortical interaction and, consequently, the generation of streamwise vorticity as observed in Fig. 4. However, at a given L_R, Re_l monotonically increases with increasing Re, indicating that ω_y decreases as Re increases. This is indeed the case for Re beyond $\mathrm{Re}_c \approx 200$ (respectively, 100) at $L_\mathrm{R} = 1.125$ (respectively, 1.25). However, a gradual increase in ω_y with increasing Re for $\mathrm{Re} < \mathrm{Re}_c$ is also observed in Fig. 4. This contradicting behavior at moderate Re may be understood by noting that the vortical interaction depends not solely on Re_l, but also on the vorticity generated at the bubble surface and at the wall. In this context, it is noted that while the surface vorticity rapidly saturates at $3U_\infty/R$, the wall vorticity at moderate Re_l is proportional to $\mathrm{Re}_l^{1/2}$. This suggests that the $\mathrm{Re}_l^{1/2}$ increase in the wall vorticity contributes significantly to the ω_y generation at moderate Re.

To better understand the relationship between vortical interactions and the generation of the streamwise vorticity, we examine the budget equation of ω_y:

$$\left(\frac{\mathrm{D}}{\mathrm{D}t} - \frac{\partial u_y}{\partial y}\right)\omega_y - \nu\nabla^2\omega_y = \omega_z\frac{\partial u_y}{\partial z} + \omega_x\frac{\partial u_y}{\partial x} = \underbrace{-\frac{\partial u_x}{\partial y}\frac{\partial u_y}{\partial z}}_{\mathrm{S}_1} + \underbrace{\frac{\partial u_z}{\partial y}\frac{\partial u_y}{\partial x}}_{\mathrm{S}_2}, \tag{7}$$

where $\mathrm{D}/\mathrm{D}t = \partial/\partial t + \boldsymbol{u}\cdot\boldsymbol{\nabla}$ represents the material derivative and $u_i = \boldsymbol{u}\cdot\boldsymbol{e}_i$ and $\omega_i = \boldsymbol{\omega}\cdot\boldsymbol{e}_i$ (with $i = x, y, z$) are projections along i of the velocity and vorticity, respectively.

In Eq. (7), the generation of ω_y is attributed to two distinct contributions, namely S_1 and S_2, which are dot products of different velocity gradients. When the flow is unbounded, the two streamwise gradients are symmetric with respect to the plane $x = 0$ and decay rapidly in the bubble wake at large but finite Re. The presence of the wall mitigates their decay, maintaining finite values for S_1 and S_2 within the lower part of the bubble wake.

Figure 5 displays the values of S_1 and S_2, and their sum in the cross-stream plane $y/R = 1/2$ at $L_\mathrm{R} = 1.125$. Alongside the vortical structure depicted in Fig. 2, S_1 is confined within the boundary layer at the bubble's lower half, while S_2 is delicate and maintains finite values within the boundary layers both at the bubble surface and the wall. Since S_1 is positive (respectively, negative) in the half-plane $z > 0$ (respectively, $z < 0$), it serves to amplify the streamwise vortex threads visible in Fig. 4. Conversely, S_2 opposes S_1, but due to its comparatively mild intensity, the sign of $\mathrm{S}_1 + \mathrm{S}_2$ mostly mirrors that of S_1. The variation of the sum with respect to Re is in accordance with that experienced by ω_y [Figs. 4(e)–4(h)]. In particular, for Re increases from 100 to 200, the maximum of $|\mathrm{S}_1 + \mathrm{S}_2|$ in the plane $y/R = 1/2$ is increased from $1.2(U_\infty R)^2$ to $1.4(U_\infty R)^2$.

IV. HYDRODYNAMIC FORCES

A. Drag force

Figure 6(a) displays the numerical results for the drag coefficient C_D as a function of the Reynolds number at various wall distances L_R. The results at $L_\mathrm{R} = 40$ align well with those in the unbounded limit, $C_{\mathrm{D}0}$, predicted using the correlation proposed in Ref. [18]. This indicates that the unperturbed far field is satisfactorily approached at a distance $r = 40R$ from the bubble center. Comparison of the results at smaller L_R with those at $L_\mathrm{R} = 40$ elucidates that the wall effects are only pronounced for $L_\mathrm{R} \leqslant 1.5$, where the drag increases rapidly with closer wall proximity, especially when Re is large.

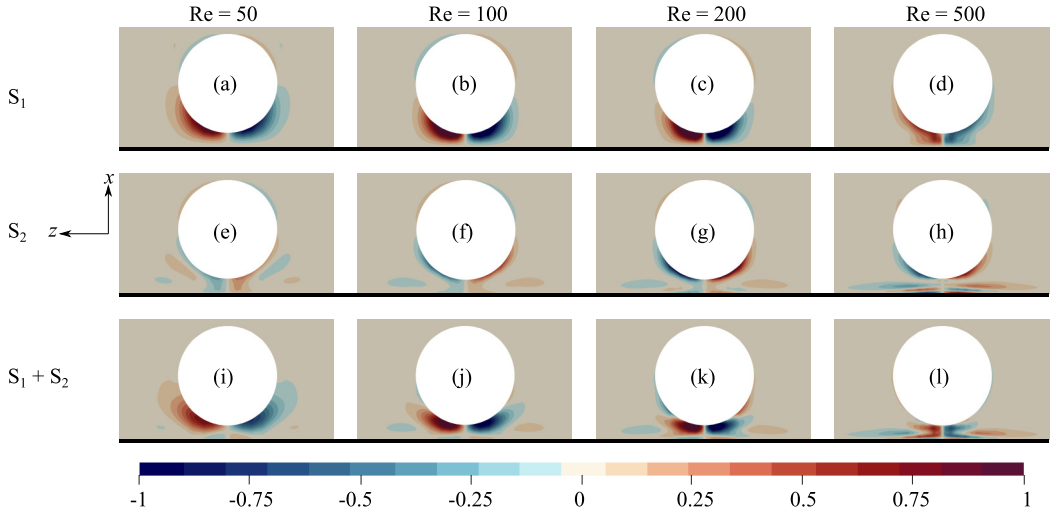

FIG. 5. Isocontours of the source terms S_1, S_2, and $S_1 + S_2$ in Eq. (7) at the cross-stream plane $y/R = 1/2$ for $L_R = 1.125$. All terms are rendered dimensionless via multiplication by $(R/U_\infty)^2$. The wall is situated at the bottom of each panel, while the relative flow with respect to the bubble is oriented inwards, along the y axis.

To highlight the drag alteration due to the wall effects, Fig. 6(b) illustrates the relative drag increase $\Delta C_D = (C_D - C_{D0})/C_{D0}$ as a function of the Reynolds number. Previous results obtained at $L_R = 1.5$ and 1.25 in Ref. [12] are also presented. It should be noted that, compared with Ref. [12], the number of grid cells used to discretize the bubble surface along the colatitudinal direction is significantly larger in the present work ($N_p \geqslant 100$ instead of $N_p = 30$; refer to the Appendix for details). From Fig. 6(b), it is evident that ΔC_D undergoes only a minor increase with increasing Re for $\mathrm{Re} \leqslant 100$. Beyond $\mathrm{Re} = 100$, ΔC_D incrementally rises with Re regardless of L_R (provided $L_R \leqslant 1.5$). These tendencies are accurately captured using the semiempirical expression proposed

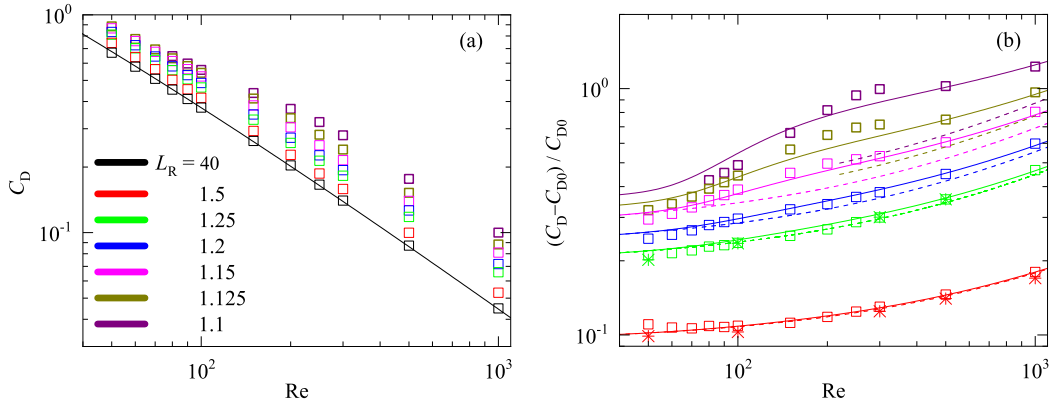

FIG. 6. Results for (a) the drag coefficient C_D and (b) the relative drag increase $(C_D - C_{D0})/C_{D0}$ as a function of the Reynolds number. In panels (a) and (b) □ denotes the present numerical results. (a) ——, semiempirical correlation $(\mathrm{Re}/16)C_{D0} = 1 + [8/\mathrm{Re} + 1/2(1 + 3.315\mathrm{Re}^{-1/2})]^{-1}$ proposed in Ref. [18]. (b) ∗, numerical results from Ref. [12]; - - - -, Eq. 8(a) with $h_D = 0$;——, Eq. 8(a) with h_D given by Eq. (8b).

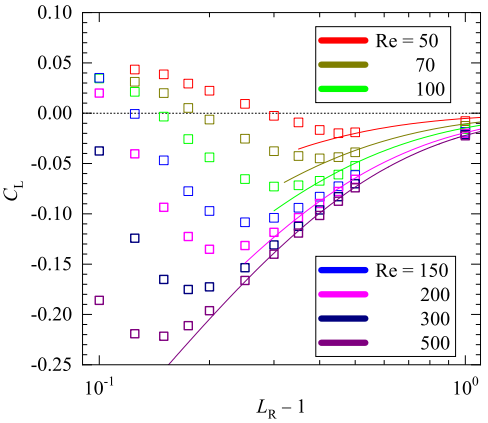

FIG. 7. Lift coefficient C_L as a function of the wall distance $L_R - 1$. □, present numerical results;——, C_L prediction from Eq. (10) with $h_L = 0$; different colors denote different Re.

in Ref. [12], derived from data for $L_R \geqslant 1.25$:

$$\Delta C_D = 0.47 L_R^{-4} + 5.5 \times 10^{-3} L_R^{-6} \mathrm{Re}^{3/4}.$$

Not surprisingly, the quantitative agreement with the present results deteriorates for $L_R < 1.2$ where ΔC_D is underestimated for $\mathrm{Re} \geqslant 100$. This underestimation may be understood by noting that the vortical interaction between the boundary layers at the wall and the bubble surface is still significant at small L_R [Figs. 2(e) and 2(f)]. Based on the present numerical results, we find it feasible to extend the previous expression to situations with L_R down to 1.1 using

$$\Delta C_D = 0.47 L_R^{-4} + 5.5 \times 10^{-3} L_R^{-6} \mathrm{Re}^{3/4} + h_D(\mathrm{Re}, L_R), \tag{8a}$$

$$h_D(\mathrm{Re}, L_R) = \exp(-7 \times 10^3 \mathrm{Re}^{-2})[1.2 \times 10^{-4} (L_R - 1)^{-7/2}]. \tag{8b}$$

As seen in Fig. 6(b), the extended expression significantly improves the agreement at smaller L_R. Throughout the ranges of parameters considered in this work, the deviation between the predicted drag coefficient using Eqs. (8) and the numerical results is always less than 5%.

B. Transverse force

Figure 7 shows the variation in the lift coefficient as a function of the wall distance for $50 \leqslant \mathrm{Re} \leqslant 500$. Note that the horizontal axis of this plot involves the quantity $L_R - 1$ because this choice is more appropriate to exhibit the rapid variation in C_L in the limit $L_R \to 1$ where the bubble comes in contact with the wall. The most striking feature revealed by this plot is that for any considered Re, the magnitude of the transverse force starts to decrease with decreasing separation when L_R is smaller than a critical value that depends on the Reynolds number. Then, when Re is not too large, there is a second critical wall distance $L_{R,C2}$ smaller than which the lift force reversals from attractive to repulsive. Our numerical results indicate that, for Re increases from 50 to 200, $L_{R,C2}$ decreases from 1.3 to around 1.1.

The reversal of the transverse force is due to the vortical interaction between the bubble and the wall as discussed in Sec. III. In particular, the two counterrotating streamwise vortices shown in Fig. 4 are known to produce a lift force directed away from the wall [19]. To better understand this vortical contribution, let us first consider the case of two identical bubbles rising side-by-side in a stagnant fluid. According to potential flow theory, each bubble experiences an attractive transverse

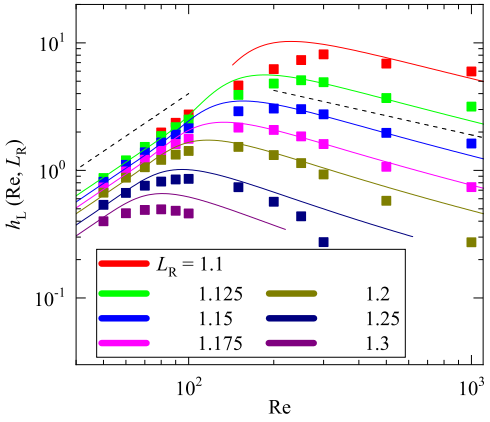

FIG. 8. Results for $h_L(\mathrm{Re}, L_R)$ as a function of the Reynolds number. Symbols: h_L computed from present numerical results; dashed lines: the $\mathrm{Re}^{3/2}$ and $\mathrm{Re}^{-1/2}$ scaling; solid lines: empirical expression Eq. (11).

force with the corresponding lift coefficient being [4,5]

$$C_{L,\mathrm{pot}} \approx -\frac{3}{8}L_R^{-4}\left(1+\frac{1}{8}L_R^{-3}+\frac{1}{6}L_R^{-5}+\frac{3}{256}L_R^{-6}+\frac{15}{128}L_R^{-7}+\frac{11}{384}L_R^{-8}\right) - \frac{3}{8}L_R^{-4}\left(\frac{65}{1024}L_R^{-9}+\frac{767}{9216}L_R^{-10}+0.3L_R^{-25}\right). \tag{9}$$

Then, at large but finite Re, weak viscous effects in the gap are known to produce a positive contribution to the lift coefficient with a magnitude of $15\mathrm{Re}^{-1}L_R^{-4}$ [6]. Although the problem considered in the present work is different from the one in Ref. [6], it still seems reasonable to treat the transverse force as a combination of two distinct contributions: one due to the irrotational mechanism and the other due to the vortical interaction. We introduce the function $h_L(\mathrm{Re}, L_R)$ such that the lift coefficient in the presence of a no-slip wall can be expressed in the form

$$C_L = C_{L,\mathrm{pot}} + 15\mathrm{Re}^{-1}L_R^{-4}[1+h_L(\mathrm{Re}, L_R)], \tag{10}$$

where $C_{L,\mathrm{pot}}$ is the potential prediction by Eq. (9). To get a first idea about the role of h_L, we compare the prediction from Eq. (10) using $h_L = 0$ with the numerical results. As seen in Fig. 7, the prediction agrees well with the numerical results obtained at large L_R where C_L is negative and decreases with decreasing L_R. However, the agreement deteriorates when C_L according to the numerical data reincreases with decreasing L_R, indicating that h_L reaches significant positive values at small L_R. We then compute h_L using Eq. (10) based on the numerical results for C_L. The obtained h_L are shown in Fig. 8 for L_R up to 1.3. For $L_R > 1.3$, the leading-order vortical contribution $15\mathrm{Re}^{-1}L_R^{-4}$ becomes small, and numerical inaccuracy in the estimated h_L cannot be excluded. We observe from Fig. 8 that h_L at a given Re increases with decreasing L_R, especially when Re is large. Conversely, at a given L_R, h_L initially increases with increasing Re and, for Re beyond a critical value that decreases with increasing L_R, redecreases as Re increases. Thus, we attempt to propose two different semiempirical expressions for h_L that are locally valid at moderate and high Reynolds numbers, respectively, and then combine them to develop a general expression. For $\mathrm{Re} \leqslant 100$, the gradual increase in h_L with increasing Re aligns with the increase in the wall vorticity, which increases as $\mathrm{Re}^{1/2}$, leading us to expect h_L to scale with $\mathrm{Re}^{3/2}$. Then, at large but finite Re ($\mathrm{Re} \geqslant 500$), the wake past the bubble does not interact significantly with the wall, and the bubble perceives the wall as a symmetry plane. In this case, weak viscous effects in the gap result in a correction to the irrotational solution [6]. Adjacent to the leading-order term, the Re correction is of $O(\mathrm{Re}^{-3/2})$, making h_L to scale with $\mathrm{Re}^{-1/2}$. The two dashed lines in Fig. 8 confirm these two

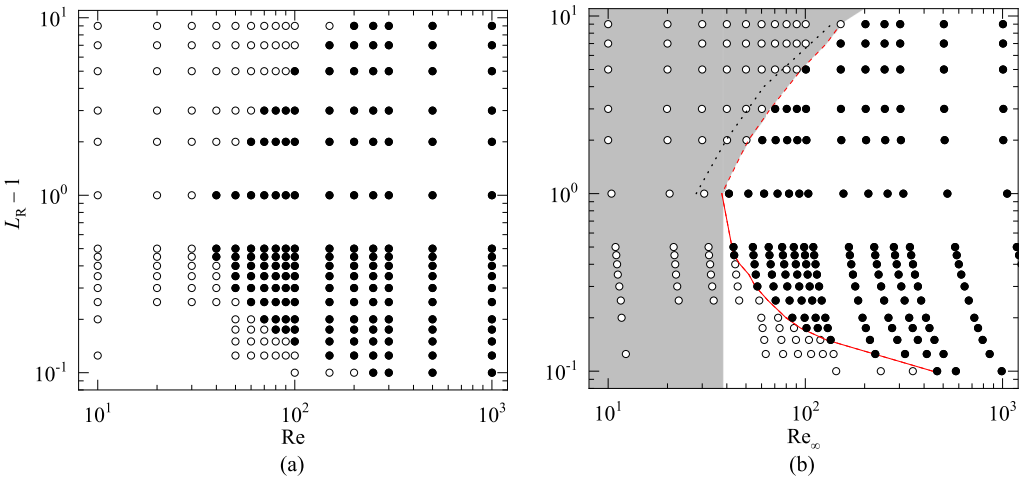

FIG. 9. Sign of the transverse force in (a) the $(\mathrm{Re}, L_\mathrm{R})$ plane and (b) the $(\mathrm{Re}_\infty, L_\mathrm{R})$ plane. •: bubbles are attracted towards the wall; ○: bubbles are repelled from the wall. (b) ——, $L_{\mathrm{R},1}(\mathrm{Re}_\infty)$; - - - -, $L_{\mathrm{R},2}(\mathrm{Re}_\infty)$; · · · · · ·, $L_{\mathrm{R},2}(\mathrm{Re}_\infty)$ obtained in Ref. [6] for two bubbles rising side-by-side; the gray area corresponds to the subregion of initial wall distance $L_{\mathrm{R,i}}$ for which the bubble migrates away from the wall up to infinity, while the white area is the basin of attraction of the stable equilibrium position $L_{\mathrm{R},1}(\mathrm{Re}_\infty)$.

scaling laws concerning Re. Based on the data at $\mathrm{Re} = 50$ and 500, we find it appropriate to scale h_L with the wall distance as L_R^{-5} at moderate Re and as $(L_\mathrm{R} - 1)^{-7/2}$ at high Re. Consequently, we propose a general expression for h_L in the form

$$h_\mathrm{L}(\mathrm{Re}, L_\mathrm{R}) = a\mathrm{Re}^{3/2}L_\mathrm{R}^{-5}c_T + b\mathrm{Re}^{-1/2}(L_\mathrm{R} - 1)^{-7/2}(1 - c_T), \quad \text{with} \tag{11a}$$

$$a = 0.0045,\ b = 0.05,\ c_T = \tanh[0.3 \times 10^5\mathrm{Re}^{-3}(L_\mathrm{R} - 1)^{-2}], \tag{11b}$$

As depicted in Fig. 8, Eq. (11) shows good agreement with the numerical results across the considered range of Re.

C. Equilibrium position

We observed in Fig. 7 that the transverse force might change its sign at a critical wall distance, provided that Re is not too large. According to our computational results, the critical Re below which this force reversal is observed is around 250. Figure 9(a) illustrates how the sign of the transverse force evolves in the plane $(\mathrm{Re}, L_\mathrm{R})$. Note that, to acquire a more general picture of this force evolution, we have extended the range of parameters by considering Re down to 10 and L_R up to 10. Given the small values of C_L for $2 \leqslant L_\mathrm{R} \leqslant 10$, two steps have been carried out to enhance the numerical accuracy in these instances. First, the computational domain along the unbounded side has been extended up to $R_\infty = 100R$ (instead of using $R_\infty = 40R$ as for cases where $L_\mathrm{R} < 2$) to avoid confinement effects. Second, the number of cells along the azimuthal direction has been doubled ($N_\varphi = 128$ instead of $N_\varphi = 64$) to further increase the resolution along φ (see the Appendix for the grid details). According to Fig. 9(a), the transverse force is always repulsive when the Reynolds number is lower than a critical value $\mathrm{Re}_\mathrm{REP} \approx 37.5$ (based on linear interpolation) corresponding to an equilibrium wall distance $L_{\mathrm{R,c}}(\mathrm{Re}_\mathrm{REP}) \approx 2$. This is consistent both with the low-Reynolds number solution [20,21], according to which the transverse force is repulsive in this Re regime irrespective of L_R, and with the experimental study of Ref. [3] where the critical Reynolds number below which the transverse force is always repulsive was found to be $\mathrm{Re}_\mathrm{REP} \approx 35$.

Our computational results facilitate addressing the fate of a bubble with a given diameter, and therefore a given Re_∞, released at an initial wall distance $L_{\mathrm{R,i}}$, moving under the effect of buoyancy. Assuming that the vertical drag force precisely balances the buoyancy force, the quantity $\mathrm{Re}^2 C_\mathrm{D}(\mathrm{Re}, L_\mathrm{R})$ remains constant, this constant being determined by the value of the Galileo number $\mathrm{Ga} = gR^3/\nu^2$, with g denoting gravity. Taken together with the drag expression in the unbounded limit proposed by Ref. [18], the map of the force evolution in the plane $(\mathrm{Re}, L_\mathrm{R})$ [Fig. 9(a)] is transformed into the plane $(\mathrm{Re}_\infty, L_\mathrm{R})$, as displayed in Fig. 9(b). A key change compared with Fig. 9(a) is that all data points with a given L_R are shifted rightwards, i.e., towards the direction where the Reynolds number increases, especially when L_R is small. This shift is due to the wall-induced drag increase discussed in Sec. IV A, which decreases the rising velocity and therefore the Reynolds number as the bubble approaches the wall.

Based on the data points in Fig. 9(b), we can construct the critical curve corresponding to $C_\mathrm{L} = 0$ by linearly interpolating the values of C_L identified in the computations. Figure 9(b) reveals that the critical curve, at which the transverse force vanishes, can be further bifurcated into two branches by the critical point $(\mathrm{Re}_{\infty,\mathrm{REP}}, L_{\mathrm{R,c}})$. These are denoted by $L_{\mathrm{R},1}(\mathrm{Re}_\infty)$ and $L_{\mathrm{R},2}(\mathrm{Re}_\infty)$, which progressively increase and decrease as Re_∞ increases, respectively. Thus, for Reynolds numbers greater than $\mathrm{Re}_{\infty,\mathrm{REP}}$ and wall distances in the considered range (i.e., $1.1 \leqslant L_\mathrm{R} \leqslant 10$), the critical curve indicates the presence of two equilibrium positions. For instance, the transverse force is found to vanish for both $L_{\mathrm{R,c}} \approx 1.175$ and ≈ 6 at $\mathrm{Re} = 50$. A meticulous inspection indicates that only the smallest of the two equilibrium values of $L_{\mathrm{R,c}}$, i.e., $L_{\mathrm{R},1}(\mathrm{Re}_\infty)$, is stable, because if the wall distance is marginally increased (respectively, decreased) above (respectively, below) $L_{\mathrm{R},1}$, the transverse force becomes attractive (respectively, repulsive), leading to a reduction of the difference $|L_\mathrm{R} - L_{\mathrm{R},1}|$. Conversely, any deviation of L_R from the larger equilibrium value $L_{\mathrm{R},2}$ tends to amplify the difference $|L_\mathrm{R} - L_{\mathrm{R},2}|$.

The computational results enable us to hypothesize about the asymptotic branches of the critical curve $L_{\mathrm{R,c}}(\mathrm{Re}_\infty)$ in the limit of both large ($L_\mathrm{R} \to \infty$) and small ($L_\mathrm{R} \to 1$) wall distances. When L_R is small, $L_{\mathrm{R,c}}(\mathrm{Re}_\infty)$ follows $L_{\mathrm{R},1}(\mathrm{Re}_\infty)$, the asymptotic behavior of which can be estimated from Eqs. (10) and (11). Given that $L_{\mathrm{R},1}$ decreases with increasing Re, for $L_\mathrm{R} \leqslant 1.1$ and $\mathrm{Re} = O(100)$, the leading-order term in h_L scales with $O(\mathrm{Re}^{-1/2}(L_\mathrm{R} - 1)^{-7/2})$, making the repulsive contribution to the transverse force to be $O(\mathrm{Re}^{-3/2}(L_\mathrm{R} - 1)^{-7/2})$. Since the irrotational contribution to C_L never exceeds unity when $L_\mathrm{R} \to 1$ [6], it is straightforward to conclude that $L_{\mathrm{R},1} - 1$ scales with $O(\mathrm{Re}^{-3/7})$. Consequently, regardless of the magnitude of Re, the lift force is expected to always reverse before the bubble contacts the wall. Notably, the slope of the curve $L_{\mathrm{R},1}(\mathrm{Re}_\infty)$ for $1.1 \leqslant L_\mathrm{R} \leqslant 1.15$ is slightly larger [about $-1/3$; see Fig. 9(b)], since the wall-induced drag increase causes Re at a given L_R to scale with Re_∞^m, where $m > 1$.

To ascertain the asymptotic behavior of $L_{\mathrm{R,c}}(\mathrm{Re}_\infty)$ in the opposite limit, $L_\mathrm{R} \to \infty$, we first recall that beyond a critical wall distance, which gradually decreases with the Reynolds number, the transverse force satisfactorily follows the irrotational solution, corrected for weak viscous effects in the gap [6]. In other words, the bubble consistently "sees" the no-slip wall as a symmetry plane in the moderate-to-high Re regime, provided that L_R is large. In Fig. 9, we also present the counterpart of the critical curve $L_{\mathrm{R},2}$, as determined in Ref. [6] for two bubbles rising side-by-side. Despite the considerable numerical uncertainty in the computations for $L_\mathrm{R} \geqslant 2$ carried out in both works, the two critical curves tend to converge at $\mathrm{Re}_\infty \approx 200$, suggesting that the vortical interaction between the boundary layers at the wall and at the bubble surface becomes negligibly small and does not affect the asymptotic behavior of the critical curve $L_{\mathrm{R},2}$ for $\mathrm{Re}_\infty \geqslant 200$. The asymptotic behavior of $L_{\mathrm{R},2}$ at large L_R has been comprehensively discussed in Ref. [6], where it is proposed that $L_{\mathrm{R},2}$ becomes independent of Re_∞ at larger, yet finite, Re_∞.

Based on the discussions above, the following scenario emerges. If a clean, spherical bubble with a sufficiently large Galileo number (such that its rise Reynolds number Re_∞ exceeds $\mathrm{Re}_{\infty,\mathrm{REP}}$) is released in a wall-bounded stagnant fluid with an initial wall distance of $L_{\mathrm{R,i}}$, then, depending on whether $L_{\mathrm{R,i}}$ is larger or smaller than $L_{\mathrm{R},2}(\mathrm{Ga})$, the bubble will either move away from the wall indefinitely or will move towards or away from the wall until it reaches the stable equilibrium

position $L_R = L_{R,1}(\mathrm{Ga})$. Conversely, if the Galileo number is too small for Re_∞ to exceed $\mathrm{Re}_{\infty,\mathrm{REP}}$, then the bubble will migrate away from the wall indefinitely, regardless of $L_{R,i}$. The subdomain corresponding to values of $L_{R,i}$, for which the bubble migrates away from the wall to infinity, is colored grey in Fig. 9(b).

D. Lateral force balance on a bouncing bubble

In most practical situations [1,3], nearly spherical clean bubbles rising at $\mathrm{Re} = O(100)$ do not remain at an equilibrium position but bounce repeatedly near the wall. This behavior has been hypothesized to be attributable to the existence of a strong transverse component of the history force, which competes with the quasisteady lift during the near-wall rising motion. The objectives of this subsection are twofold: (1) to evaluate the significance of the history force in a repetitive near-wall bubble motion and (2) to ascertain if its magnitude can be approximated using the low-Reynolds number solution. To check the significance of the history effects, we examine the evolution of various transverse forces on a bubble undergoing near-wall bouncing motion. Following Ref. [3], the transverse force balance on a bouncing bubble may be approximately formulated as

$$\underbrace{\frac{4}{3}\pi R^3 \rho C_M \left(-\frac{dW}{dt}\right)}_{\text{Added mass}} + \underbrace{4\pi\mu R(-W)h(\mathrm{Re})(1+C_{ww})}_{\text{Lateral drag}} + \underbrace{4\pi\mu R \int_{-\infty}^{t} K(t-\tau)\left(-\frac{dW}{d\tau}\right)d\tau}_{\text{History force}} + \underbrace{\pi R^2 \rho C_L \frac{U^2}{2}}_{\text{Lift}} = 0. \tag{12}$$

In Eq. (12), C_M is the added mass coefficient corresponding to a sphere moving perpendicularly to a plane, C_{ww} represents the near-wall correction to the quasisteady drag force, $h(\mathrm{Re})$ signifies the finite-Re drag correction in an unbounded uniform stream, W and U are the instantaneous bubble velocities along the wall-normal and the streamwise directions, respectively, and $K(t-\tau)$ is the kernel of the history contribution. The added mass coefficient can be reasonably approximated using [22]

$$C_M = 0.5 + 0.2182 L_R^{-3.21} + 0.081 L_R^{-19}.$$

For the finite-Re drag correction, the semiempirical expression from Ref. [18] can be utilized:

$$h(\mathrm{Re}) = 1 + \left[\frac{8}{\mathrm{Re}} + \frac{1}{2}(1 + 3.315\mathrm{Re}^{-1/2})\right]^{-1}.$$

Analytical solutions for C_{ww} have been obtained in the Stokes flow limit [20], and in that of a viscous irrotational flow [23]. In both asymptotic limits, the wall-induced correction to the drag of a bubble moving perpendicularly to the wall is twice that on a bubble moving parallel to it. To obtain a reasonable estimate of C_{ww} at finite Re, we assume that this property holds whatever Re, namely $C_{ww} = 2\Delta C_D$ with ΔC_D given in Eq. (8). Last, C_L can be estimated based on Eqs. (10) and (11). The only unknown in Eq. (12) is the expression for the kernel $K(t-\tau)$. However, since all the rest terms are known *a priori*, the history force can be estimated based on the force balance Eq. (12).

As a typical example, we consider the experiment of Ref. [3] where they observed the near-wall bouncing motion of a bubble with $R = 0.385$ mm and $\mathrm{Re}_\infty = 130$. The bubble trajectory along the wall-normal direction was found to be satisfactorily fitted using

$$L_R(t) = \varepsilon_0 + \varepsilon \sin(\omega t) \quad \text{with} \varepsilon_0 = 1.3, \quad \varepsilon = 0.256, \quad \omega = 60.6.$$

This yields

$$W(t) = \varepsilon\omega R \cos(\omega t) \quad \text{and} \quad \frac{dW}{dt} = \varepsilon\omega^2 R \sin(\omega t).$$

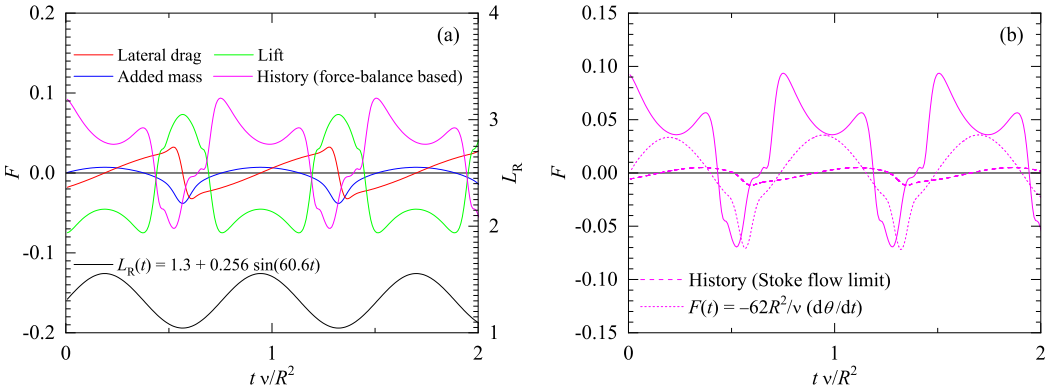

FIG. 10. Results for the various hydrodynamic forces on a bubble bouncing close to the wall. In panel (a), the left tick label corresponds to the force normalized by $\pi R^2\rho U^2/2$, while the right one corresponds to the wall distance L_R. In panel (b), different lines correspond to the estimated history force based on different methods. Results for the bubble trajectory were originally presented in the experiment of Ref. [3]. Details about the experimental condition: $\nu = 1.08 \times 10^{-6}\mathrm{m}^2/\mathrm{s}$, $R = 0.385\,\mathrm{mm}$, and $\mathrm{Re}_\infty = 130$.

Assuming that the buoyancy is always balanced by the vertical drag, $U(t)$ can be obtained based on

$$\mathrm{Re}_U^2 C_D(\mathrm{Re}_U, L_R) = \mathrm{Re}_\infty^2 C_{D0}(\mathrm{Re}_\infty), \tag{13}$$

where Re_U is the bubble Reynolds number based on $U(t)$. The Reynolds number based on the mean rising velocity $\overline{U}$ [with $\overline{U} = \frac{1}{T}\int_0^t U(t)dt$ and $U(t)$ estimated from Eq. (13)] is around 101, which is close to the measured value 96.25.

Results for the various interfacial forces on the bubble undergoing a bouncing motion outlined above are shown in Fig. 10(a). To make the comparison with C_L easily, all forces are normalized by $\pi R^2\rho U^2/2$. We note that the sign of C_L reverses at $L_R \approx 1.15$ together with a local Reynolds number [based on $U(t)$] of $\mathrm{Re} \approx 100$. In most cases, the added mass and the lateral drag are too small and it is the history force that competes energetically with the lift.

The Reynolds number based on the mean migration velocity $\overline{W}$ is around 2.5. It is therefore tempting to check if the history force estimated above could be reasonably reproduced by the analytical solution achieved in the Stokes flow limit [24]. The kernel of the history contribution in this limit takes the form

$$K(t-\tau) = 2\,\mathrm{erfc}[3(\nu(t-\tau)/R^2)^{1/2}]\exp(9\nu(t-\tau)/R^2).$$

Figure 10(b) compares the predicted history force in the Stokes flow limit with the one based on the force balance Eq. (12). The low-Re solution is an order of magnitude smaller than that estimated from Eq. (12), indicating that the lateral development of the surface vorticity does not play a key role in generating the transverse component of the history force.

Another origin of the history force relates to the time-dependent misalignment between the wake and the instantaneous angle of the bubble path, which necessarily results in a lateral force [25,26]. Indeed, in the case considered above the dimensionless radian frequency $\omega R^2/\nu$ is about 8.3, implying that the frequency of the lateral motion is too high for the bubble wake to be perfectly aligned at all times with the bubble velocity. To provide a qualitative estimation of the resulting history force, we note that the instantaneous angle of the bubble path is $\theta(t) = \tan^{-1}[W(t)/U(t)]$, and the dimensionless history force due to the misalignment is roughly proportional to $-d\theta/dt$. We see from Fig. 10(b) that the time evolution of $-d\theta/dt$ satisfactorily follows that of the history force estimated from the force balance Eq. (12). Quantitatively, a reasonable agreement can be achieved using the fitted expression $F(t) = -62(R^2/\nu)d\theta/dt$. A general and more accurate expression for the history force may be obtained by treating the prefactor as a function of the instantaneous

Reynolds number and the wall distance, provided that more accurate and more comprehensive data for the bouncing motion are available.

V. SUMMARY AND CONCLUDING REMARKS

In this work, we have studied numerically the hydrodynamic force experienced by a clean spherical bubble moving parallel to a wall at moderate-to-high Reynolds numbers. By considering the wall distance down to $L_R = 1.1$, we were able to reproduce a striking behavior already reported in several laboratory experiments. Namely, when the wall distance is sufficiently small, the direction of the transverse force on the bubble may reverse from attractive to repulsive. The mechanism responsible for the reversal of the transverse force is twofold. First, smaller than a critical Re-dependent wall distance, the acceleration of the streamwise flow in the gap is suppressed by the strong vortical wall-bubble interaction (Figs. 2 and 3). Consequently, the wall-proximity decreases the pressure gradient in the gap and, hence, the attractive contribution to the transverse force by the irrotational mechanism. Second, the strong shear flow in the gap, combined with the local transverse gradient of the streamwise velocity, results in a pair of counterrotating streamwise vortices in the bubble wake (Figs. 4 and 5), causing a "shear-induced" lift force [19]. The two processes act in a cooperative manner and contribute to produce a repulsive transverse force, making the combined lift force reverses from attractive (corresponding to the irrotational mechanism) to repulsive (corresponding to the above vortical mechanism) when the wall distance is smaller than a critical Re-dependent value.

Based on the results for the drag and lift forces obtained, we examined, in the absence of any history effects, the fate of a clean spherical bubble rising close to a wall in a stagnant fluid. Our computational results showed that bubbles with a Reynolds number lower than a critical value of $\mathrm{Re}_{\infty,\mathrm{REP}} \approx 37.5$ are repelled away from the wall regardless of the initial wall distance $L_{R,i}$, while at higher Reynolds number, bubbles are repelled from the wall up to infinity only if they are released with a separation $L_{R,i}$ larger than a critical value $L_{R,2}(\mathrm{Re}_\infty)$. In the opposite case where $L_{R,i}$ is smaller than $L_{R,2}(\mathrm{Re}_\infty)$, bubbles tend to reach an equilibrium position corresponding to a wall distance $L_R = L_{R,1}(\mathrm{Re}_\infty)$ with $L_{R,1}(\mathrm{Re}_\infty) < L_{R,2}(\mathrm{Re}_\infty)$, $L_{R,1}$ being a decreasing function of the Reynolds number, which is about 2 (corresponding to a separation distance about one bubble radius) for $\mathrm{Re}_{\infty,\mathrm{REP}} \approx 37.5$.

Finally, based on the trajectory of a near-wall bouncing bubble reported in previous experiments, the lateral force balance on a bouncing bubble was examined, based on which the crucial role of the history effects in reproducing the bouncing motion was confirmed. More precisely, we showed that the history force closely relates to the misalignment between the wake and the instantaneous angle of the bubble path and cannot be described by the analytical solution achieved in the Stokes flow limit, although the Reynolds number based on the migration velocity is only $O(1)$.

From a practical point of view, the present results provide empirical models for the drag [Eqs. (8)] and the transverse force [Eqs. (10) together with Eqs. (9) and (11)] acting on nearly spherical bubbles for $L_R \geqslant 1.1$ and $\mathrm{Re} \geqslant 50$. These models can be easily merged with their counterparts in the low-to-moderate Re regime developed in Ref. [12] to achieve more general ones that are valid irrespective of Re (provided that the bubbles are still nearly spherical). These extended models, together with the ones accounting for the inhomogeneity of the ambient flow (see, e.g., Ref. [27]) and the pairwise bubble interactions [6,28], may be used in practical calculations to estimate the averaged characteristics of the overall flow, especially to determine the lateral distribution of bubbles in pipe and channel flows. Nevertheless, it must be kept in mind that the transient trajectory of bubbles undergoing bouncing motion cannot be properly predicted without an accurate model for the transverse history force. Full numerical simulations, possibly including effects of deformation, are highly desirable to obtain more accurate and more complete variations of the lift force and of the transverse history force over the full range of Reynolds number and wall distance.

The cause of the lateral history force triggering the repeatable near-wall bouncing motion remains an open question from this work. Prior studies [29,30] on zigzagging motions of clean bubbles in

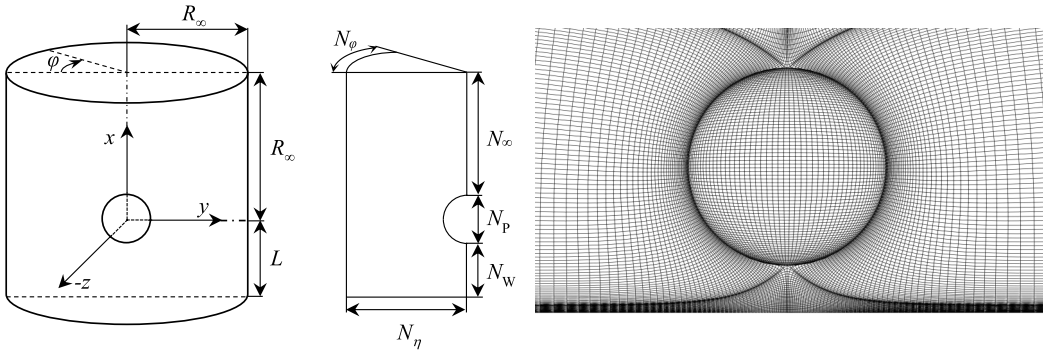

FIG. 11. Illustration of the grid system: (a) Shape and size of the computational domain. (b) Definition of the number of nodes in the computational domain. (c) Partial view of the grid in the plane $z = 0$ and on the bubble surface in the case $L_R = 1.25$, with grid details outlined in Table I.

unbounded fluids have highlighted the connection between the wake instability and path instability. Yet, in wall-bounced configurations, the wake past a fixed bubble remains stable for Re up to 1000 and L_R down to 1.1, as confirmed from this work. This suggests a different mechanism for the path instability in wall-bounded situations compared to the unbounded case, where wake instability is primarily due to the excess vorticity on the bubble surface. Future work in acquiring the three-dimensional wake structure of a deformable bubble rising freely in a wall stagnant liquid is crucial to understand the physical origin of the lateral history force.

ACKNOWLEDGMENTS

This work was funded by the Deutsche Forschungsgemeinschaft (DFG, German Research Foundation) (P.S., Grant No. 501298479). We thank J. Magnaudet for engaging in insightful discussions regarding the history effects in near-wall bouncing motion and for his generous permission and guidance in utilizing the JADIM code. Additionally, we acknowledge the extensive technical support provided by H. Schulz and N. Elkina for the simulations conducted on the HPC cluster *hemera* at HZDR.

APPENDIX: GRID STUDY

The grid system employed in this study is similar to those used in previous works [12,13]. Figure 11 delineates the computational domain as cylindrical [Fig. 11(a)], formed by rotating a two-dimensional surface about the x axis through an angle $\varphi = 2\pi$. This domain extends both in the streamwise (upstream and downstream) and cross-stream directions on the unbounded side, spanning a distance R_∞. The no-slip wall is represented by the cylinder's bottom surface, coinciding with the horizontal plane $x = -L$. Discretization of the computational domain utilizes $(N_w + N_p + N_\infty) \times N_\infty \times N_\varphi$ cells along the axial, radial, and azimuthal directions, respectively [see Fig. 11(b)]. Figure 11(c) illustrates the spatial distribution of the grid cells in the symmetry plane $z = 0$ and on the bubble surface $r = R$. While cells on the bubble surface are uniformly distributed along the polar and azimuthal directions, those in the gap and along the unbounded side are nonuniformly distributed to enhance the resolution within the boundary layers at the wall and bubble surface.

The grid system involves two lengthscales crucial for accurate numerical simulations. The first is the distance from the bubble center to the outer boundary of the computational domain. At moderate-to-high Reynolds numbers, as considered in this work, it has been shown [12] to be sufficient to

TABLE I. Grid details at different wall distances L_R.

L_R	R_∞/R	δ/R	N_p	N_w	N_∞	N_φ
[1.1, 1.15]	40	5×10^{-5}	200	20	84	64
[1.175, 1.25]	40	1.5×10^{-4}	150	20	84	64
[1.3, 1.5]	40	2×10^{-4}	100	30	84	64
[2, 10]	100	1×10^{-3}	100	40	84	128

position the outer boundary at $R_\infty = 40R$ to mitigate confinement effects. This configuration is utilized in the present work for $L_R < 2$, while $R_\infty = 100R$ is applied for cases involving larger wall distances. The second scale is the thickness, δ, of the cell nearest to the point $(x = 0, y = -R, z = 0)$. This thickness must be minimized to ensure adequate resolution of the flow in the boundary layers at both the bubble surface and the wall. The first dependency is predictable, and satisfactory grid resolution can be achieved provided $\delta/R \leqslant 0.002$ [12]. The latter dependency arises because the 2D grid in the symmetry plane $z = 0$ is constructed based on the streamlines $\eta =$ const. and the equipotential lines $\xi =$ const. of the potential flow around two circular cylinders moving in line along the x axis. Consequently, using such a 2D grid means that, with a given δ, the radial length of the cells nearest to the two polar points $(x = \pm R, y = 0, z = 0)$, say δ_r, increases with decreasing L_R. As listed in Table I, in this work, δ is set as $0.001R$ for $L_R \geqslant 2$ and is progressively decreased with decreasing L_R such that $\delta_r/(L - R) \leqslant 0.1$ is satisfied for all considered L_R.

Based on the settings for δ and R_∞ mentioned above, we tested different number of nodes $(N_w, N_p, N_\infty, N_\varphi)$ at various wall distances and analyzed the impact of these numbers on the computed drag and lift forces. Table I summarizes the desirable values for N_p, N_w, N_∞, and N_φ that are determined by the grid study. The accuracy of the predicted drag modification and the transverse force due to the wall effects largely depends on the sufficiency of the resolution in the gap. In this context, our previous work demonstrated that $N_w = 30$ (or 40) is sufficient for $L_R = 1.5$ (or 2). We conducted further tests at smaller wall distances; some typical results are summarized in cases a1–a4 in Table II. To achieve reasonable resolution inside the gap, it is necessary to have $N_w = 20$ for $L_R \leqslant 1.25$ and $N_w = 30$ for $1.3 \leqslant L_R \leqslant 1.5$. The distribution of these N_w grid points

TABLE II. Effect of the number of nodes of (a) N_w, (b) N_∞, and (c) N_φ on the drag and lift forces. The rest grid details are identical as those listed in Table I.

Case			Re = 50		Re = 500	
(a)	L_R	N_w	C_L	C_D	C_L	C_D
*a*1	1.25	30	0.009	0.811	−0.166	0.118
*a*2	1.25	20	0.009	0.811	−0.165	0.117
*a*3	1.125	20	0.043	0.885	−0.219	0.152
*a*4	1.125	10	0.042	0.886	−0.220	0.152
(b)	L_R	N_∞	C_L	C_D	C_L	C_D
*b*1	1.125	56	0.041	0.882	−0.196	0.152
*b*2	1.125	84	0.043	0.885	−0.219	0.152
*b*3	1.125	112	0.043	0.886	−0.219	0.152
(c)	L_R	N_φ	C_L	C_D	C_L	C_D
*c*1	1.2	32	0.028	0.840	−0.198	0.127
*c*2	1.2	64	0.022	0.834	−0.196	0.126
*c*3	1.2	128	0.022	0.833	−0.196	0.126

in the gap is significantly influenced by N_p. This is because, in the current grid system, the axial length of the cell nearest to the polar point ($x = -R$, $y = 0$, $z = 0$), denoted as δ_x, is comparable with the polar length of the grid cells on the bubble surface, i.e., $\delta_x \approx \pi R/N_p$. We used larger N_p at smaller L_R so that, for all considered L_R, approximately 10 grid points are clustered within the wall boundary layer at $\mathrm{Re} = 500$. The grid resolution inside the bubble wake is largely affected by the number of cells along the radial direction, i.e., N_∞, and the thickness δ. With a smaller δ, more grid points are clustered in the region closer to the bubble and, consequently, only limited grid points are distributed in the bubble wake. The most challenging cases are those for $L_R \leqslant 1.15$ where δ/R is only 5×10^{-5}. To ensure that the bubble wake is reasonably resolved, we increased N_∞ from 56 to 112 and found it sufficient to set $N_\infty = 84$ (cases b1–b3 in Table II). Finally, to assess the grid resolution along the azimuthal direction, we increased N_φ from 32 to 128 (cases c1–c3 in Table II) at several different wall distances and found that $N_\varphi = 64$ always allows sufficient resolution for $L_R < 2$. At larger wall distances, $N_\varphi = 128$ is used to further improve the accuracy in the calculated C_L.

[1] A. W. G. de Vries, Path and wake of a rising bubble, Ph.D. dissertation, University of Enschede, 2001.

[2] S. Hosokawa, A. Tomiyama, S. Misaki, and T. Hamada, Lateral migration of single bubbles due to the presence of wall, in *Proceedings of the Fluids Engineering Division Summer Meeting* (ASME, New York, NY, 2002).

[3] F. Takemura and J. Magnaudet, The transverse force on clean and contaminated bubbles rising near a vertical wall at moderate Reynolds number, J. Fluid Mech. **495**, 235 (2003).

[4] L. Van Wijngaarden, Hydrodynamic interaction between gas bubbles in liquid, J. Fluid Mech. **77**, 27 (1976).

[5] T. Miloh, Hydrodynamics of deformable contiguous spherical shapes in an incompressible inviscid fluid, J. Eng. Math. **11**, 349 (1977).

[6] D. Legendre, J. Magnaudet, and G. Mougin, Hydrodynamic interactions between two spherical bubbles rising side by side in a viscous liquid, J. Fluid Mech. **497**, 133 (2003).

[7] K. I. Sugioka and T. Tsukada, Direct numerical simulations of drag and lift forces acting on a spherical bubble near a plane wall, Int. J. Multiphase Flow **71**, 32 (2015).

[8] G. Mougin and J. Magnaudet, Wake-induced forces and torques on a zigzagging/spiralling bubble, J. Fluid Mech. **567**, 185 (2006).

[9] R. Zenit and D. Legendre, The coefficient of restitution for air bubbles colliding against solid walls in viscous liquids, Phys. Fluids **21**, 083306 (2009).

[10] H. Jeong and H. Park, Near-wall rising behaviour of a deformable bubble at high Reynolds number, J. Fluid Mech. **771**, 564 (2015).

[11] A. Tiwari, C. Pantano, and J. B. Freund, Growth-and-collapse dynamics of small bubble clusters near a wall, J. Fluid Mech. **775**, 1 (2015).

[12] P. Shi, R. Rzehak, D. Lucas, and J. Magnaudet, Hydrodynamic forces on a clean spherical bubble translating in a wall-bounded linear shear flow, Phys. Rev. Fluids **5**, 073601 (2020).

[13] P. Shi, R. Rzehak, D. Lucas, and J. Magnaudet, Drag and lift forces on a rigid sphere immersed in a wall-bounded linear shear flow, Phys. Rev. Fluids **6**, 104309 (2021).

[14] J. Magnaudet, M. Rivero, and J. Fabre, Accelerated flows past a rigid sphere or a spherical bubble. Part 1. Steady straining flow, J. Fluid Mech. **284**, 97 (1995).

[15] I. Calmet and J. Magnaudet, Large-eddy simulation of high-Schmidt number mass transfer in a turbulent channel flow, Phys. Fluids **9**, 438 (1997).

[16] D. Legendre and J. Magnaudet, The lift-force on a spherical bubble in a viscous linear shear flow, J. Fluid Mech. **368**, 81 (1998).

[17] A. Blanco and J. Magnaudet, The structure of the axisymmetric high-Reynolds number flow around an ellipsoidal bubble of fixed shape, Phys. Fluids **7**, 1265 (1995).

[18] R. Mei, J. F. Klausner, and C. J. Lawrence, A note on the history force on a spherical bubble at finite Reynolds number, Phys. Fluids **6**, 418 (1994).
[19] T. R. Auton, The lift force on a spherical body in a rotational flow, J. Fluid Mech. **183**, 199 (1987).
[20] F. Takemura, S. Takagi, J. Magnaudet, and Y. Matsumoto, Drag and lift forces on a bubble rising near a vertical wall in a viscous liquid, J. Fluid Mech. **461**, 277 (2002).
[21] J. Magnaudet, S. Takagi, and D. Legendre, Drag, deformation and lateral migration of a bouoyant drop moving near a wall, J. Fluid Mech. **476**, 115 (2003).
[22] A. A. Kharlamov, Z. Chára, and P. Vlasák, Hydraulic formulae for the added masses of an impermeable sphere moving near a plane wall, J. Eng. Math. **62**, 161 (2008).
[23] J. B. W. Kok, Dynamics of a pair of gas bubbles moving trough liquid. 1. Theory, Eur. J. Mech. B-Fluids **12**, 515 (1993).
[24] S. Yang and L. G. Leal, A note on memory-integral contributions to the force on an accelerating spherical drop at low Reynolds number, Phys. Fluids **3**, 1822 (1991).
[25] F. Candelier, B. Mehlig, and J. Magnaudet, Time-dependent lift and drag on a rigid body in a viscous steady linear flow, J. Fluid Mech. **864**, 554 (2019).
[26] P. Shi, V. Tholan, A. E. Sommer, S. Heitkam, K. Eckert, K. Galvin, and R. Rzehak, Forces on a nearly spherical bubble rising in an inclined channel flow, Int. J. Multiph. Flow **169**, 104620 (2023).
[27] J. Magnaudet and I. Eames, The motion of high-Reynolds-number bubbles in inhomogeneous flows, Annu. Rev. Fluid Mech. **32**, 659 (2000).
[28] Y. Hallez and D. Legendre, Interaction between two spherical bubbles rising in a viscous liquid, J. Fluid Mech. **673**, 406 (2011).
[29] J. Magnaudet and G. Mougin, Wake instability of a fixed spheroidal bubble, J. Fluid Mech. **572**, 311 (2007).
[30] J. C. Cano-Lozano, C. Martinez-Bazan, J. Magnaudet, and J. Tchoufag, Paths and wakes of deformable nearly spheroidal rising bubbles close to the transition to path instability, Phys. Rev. Fluids **1**, 053604 (2016).